

POWER QUALITY ENHANCEMENT FOR A GRID CONNECTED WIND TURBINE ENERGY SYSTEM

Mr. P.Mallikarjun ^{1*}

Assistant Professor, Dept. of EEE
St. Peters Engineering College, Hyderabad, India
mallikarjun@stpetershyd.com

M.Harikrishna²

UG Scholar, Dept. of EEE
St. Peters Engineering College, Hyderabad, India
harikrishnamateti07@gmail.com

M.Sriharsha ³

UG Scholar, Dept. of EEE
St. Peters Engineering College, Hyderabad, India
mugalasriharsha@gmail.com

Mohd Abdul Sami⁴

UG Scholar, Dept. of EEE
St. Peters Engineering College, Hyderabad, India
sami868693@gmail.com

B.Varun Joseph ⁵

UG Scholar, Dept. of EEE
St. Peters Engineering College, Hyderabad, India
varunjosephb@gmail.com India

ABSTRACT- This paper discusses a comprehensive control of a wind turbine system connected to an industrial facility. An algorithm has been developed that enables a control structure to inject the available energy while also acting as an active power filter to reduce load current disturbances and improve power quality. We take into account a four-wire system with linear and nonlinear three-phase, single-phase, and three-phase loads. The utility-side controller is intended to correct for disruptions generated by reactive, nonlinear, and/or unbalanced single- and intra-phase loads during the connection of the wind turbine in addition to supplying active and reactive electricity as needed. The controller is inactive when there is no wind power available. The power quality will be improved by the controller employing the grid-connected power converter and dc-link capacitor. The proposed control structure is based on the conservative power theory decompositions, which is the major distinction between the proposed methodology and others in the literature. This option offers very flexible, discerning, and potent functionalities by providing separated power and current references for the inverter control. In order to assess the performance of the suggested control algorithm for complete real-time implementation, real-time software benchmarking has been done. The outcomes supported our power quality enhancement control and permitted the exclusion of passive filters, making the electronic implementation of a smart-grid based control more portable, adaptable, and dependable.

Keywords—Conservative power theory (CPT), permanent magnet synchronous generator (PMSG), four-leg voltage source converter (VSC), hardware-in-the-loop (HIL), and power quality, Matlab2016a.

I.INTRODUCTION

In the last few years, the global capacity of installed wind turbulences has rapidly increased. by 2013, there were around 300 gw of installed wind capacity. The following Submitted on May 15, 2016, updated on October 3, 2016, and approved on December 18, 2016. Published on January

24, 2017, the most recent version was released on May 18, 2017, With comparable costs in \$/kWh when compared to conventional fossil fuel power plants, the wind turbine sector has experienced great growth, supporting this energy source as a mainstream renewable resource. The improvement in electrical generators and power electronics is to blame for this growth. The primary problem with renewable energy is that it sometimes runs out when it's required. Power electronic inverters are used to control active/reactive power, frequency, and to support grid voltage during failures and voltage sags as a result of utility integration, which has been created and put into practice. For standalone and grid-connected wind turbine systems, a number of control strategies have been developed. The active and reactive power is sent to the grid with the help of the grid side controllers, Different power theories have been put forth and used in electrical power systems to examine current and voltage components in order to support the theoretical framework, such as the instantaneous power (PQ) theory for a three-phase system developed by Akagi. To more simply express active and reactive components, the three-phase reference frame in PQ theory is converted into a two-phase reference frame. The conservative power theory (CPT), a three-phase power theory with a broader perspective, has been developed. In this theory, the current and voltage components are obtained in the three-phase form without the need for reference-frame transformation. These ideas' effectiveness has been contrasted. Using the CPT as an alternative to generating different current references for selective disturbances compensation, where both single-phase and three-phase loads are fed, this paper suggests a control structure in three-phase four-wire systems that adds functionality to the grid-side converter of a wind turbine system. Utilizing traditional three-leg converters with "split-capacitor" technology or four-leg converters, three-phase, four-wire inverters have been produced. The ac neutral wire is directly connected to the electrical midway of the dc bus in a three-leg conventional converter. The ac neutral wire connection in a four-leg converter is made through the fourth switch leg. Better controllability is provided by the "four-leg" converter topology.

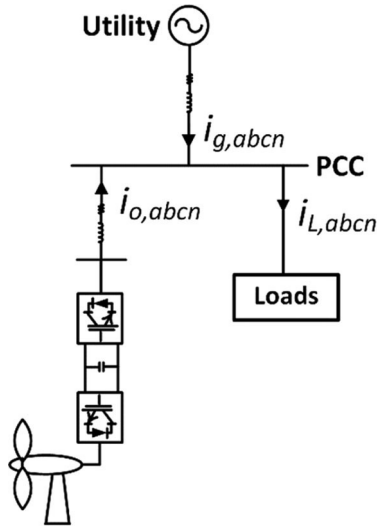


Fig. 1. Single line diagram of the addressed industrial system with wind turbine system.

The considered system consists of single- and three-phase linear and nonlinear (balanced and unbalanced) loads. The CPT is used to identify and to quantify the amount of resistive, reactive, unbalanced, and nonlinear characteristics of a particular load under different supply voltages condition for four-wire system. This paper is the journal version of our presented work in the 2015 Industry Applications Society (IAS) Annual Meeting [20].

The organization of the paper is as follows. Section II presents the utility-connected wind turbine system considered in this paper. In Section III, a brief review of the CPT for three-phase circuits is presented. Section IV presents the control design of the back-to-back converter system. Section V is dedicated to the experimental verification of the proposed control structure through a real-time hardware-in-the-loop (HIL) setup. Finally, the conclusion of this paper is presented in Section VI.

I. SYSTEM CONFIGURATION

Fig. 1 shows a diagram of a utility connected industrial system addressed in this paper. The structure of the power converter used in the wind turbine system is a back-to-back converter with a permanent magnet synchronous generator (PMSG) connected to the same bus with the loads. The loads are a combination of linear and highly inductive loads causing harmonics at the point of common coupling (PCC).

The model of the wind turbine system considered in this paper is described. The generator of the system is based on the PMSG.

II. CONSERVATIVE POWER THEORY

The CPT decomposes the power and current in the stationary frame, according to terms directly related to electrical characteristics, such as average power transfer, reactive energy, unbalanced loads and nonlinearities. Assuming a generic poly-phase circuit under periodic operation (period T), where \underline{v} and \underline{i} are, respectively, the voltage and current

vectors, and $\langle \underline{v} \rangle$ is the unbiased integral of the voltage vector measured at a given network port (phase variables are indicated with subscript “ m ”), the CPT authors define .

1) Instantaneous active power

$$p(t) = \underline{v} \cdot \underline{i} = \sum_{m=1}^M v_m i_m. \quad (1)$$

2) Instantaneous reactive energy

$$w(t) = \underline{v}^\wedge \cdot \underline{i} = \sum_{m=1}^M \hat{v}_m i_m. \quad (2)$$

The corresponding average values of (1) and (2) are the active power and reactive energy defined in (3) and (4), respectively as follows:

$$P = \overline{p} = \underline{v} \cdot \underline{i} = \frac{1}{T} \int_0^T \underline{v} \cdot \underline{i} dt = \sum_{m=1}^M P_m, \quad (3)$$

$$W = \overline{w} = \underline{v}^\wedge \cdot \underline{i} = \frac{1}{T} \int_0^T \hat{v} \cdot i dt = \sum_{m=1}^M W_m. \quad (4)$$

The phase currents are decomposed into three current components as follows.

Active phase currents are defined by

$$i_{am} = \frac{v_m i_m}{\|v_m\|^2} v_m = \frac{P_m}{V_m^2} v_m = G_m v_m, \quad (5)$$

where (G_m) is the equivalent phase conductance.

Reactive phase currents are given by

$$i_{rm} = \frac{\hat{v}_m i_m}{\|\hat{v}_m\|^2} \hat{v}_m = \frac{W_m}{\hat{V}_m^2} \hat{v}_m = B_m \hat{v}_m, \quad (6)$$

where (B_m) is the equivalent phase reactivity.

Void phase currents are the remaining current terms

$$i_{vm} = i_m - i_{am} - i_{rm}, \quad (7)$$

where they convey neither active power nor reactive energy.

The active and reactive phase currents can be further decomposed into balanced and unbalanced terms.

The balanced active currents have been defined as

$$i_{am}^b = \frac{\underline{v} \cdot \underline{i}}{\|\underline{v}\|^2} v_m = \frac{P}{V^2} v_m = G^b v_m, \quad (8)$$

and such currents represent the minimum portion of the phase currents, which could be associated with a balanced equivalent circuit, responsible for conveying the total active power (P) in the circuit, under certain voltage conditions.

The balanced reactive currents have been defined as

$$i_{rm}^b = \frac{\underline{v}^\wedge \cdot \underline{i}}{\|\underline{v}^\wedge\|^2} \hat{v}_m = \frac{W_r}{\hat{V}^2} \hat{v}_m = B^b \hat{v}_m, \quad (9)$$

and they represent the minimum portion of the phase currents, which could be associated with a balanced equivalent circuit, responsible for conveying the total reactive energy (W) in the circuit.

The imbalanced active currents are calculated by difference between (5) and (8)

$$i_{am}^u = i_{am} - i_{am}^b = G_m - G^b v_m. \quad (10)$$

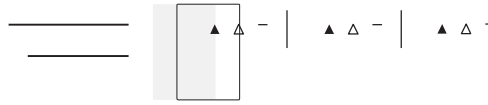


Fig. 4. Schematic diagram of the configurable load in Fig. 3.

TABLE II
GRID SIDE SYSTEM AND LOAD PARAMETERS

Parameters	Values
Nominal grid pick phase voltage, v_{pcc}	180 V
Grid frequency, f	60 Hz
Switching frequency, f_s	12 kHz
Output filter inductor, L_f	10 mH
Output filter resistor, R_f	0.1 Ω
DC link voltage reference, V_{dc}	1000 V
DC-link capacitor, C_{dc}	5 mF
Grid inductor, L_g	3 mH
Grid resistor, R_g	1 Ω
Load inductor, L_1	30 mH
Load inductor, L_2	4 mH
Load capacitor, C_1	220 μ F
Load resistor, R_1	1 Ω
Load resistor, R_2	80 Ω
Load resistor, R_3	35 Ω
Load resistor, R_4	30 Ω
Load resistor, R_5	40 Ω
Load resistor, R_6	200 Ω
Load resistor, R_7	150 Ω
Load resistor, R_8	200 Ω

of the ac-side currents $i_{o,abcn}(t)$ are described by (16) and (17). Equation (16) represents a system in which $i_{o,abcn}(t)$ are the state variables, $v_{o,abcn}(t)$ are the control inputs, and $v_{pcc,abcn}(t)$ are the disturbance inputs. Based on (17), the control input $v_{o,abcn}(t)$ are proportional to, and can be controlled by, the modulating signal $m_{o,abcn}(t)$. The transfer function of the current control scheme, $G_i(s)$, is determined as in (18). The first step to perform the controller design is to obtain the open-loop current transfer function $G_{oi}(s)$ as expressed in (19) with $C_i(s)$ the controller of the current control loop, consisting of a lag compensator as (20), where the parameters of

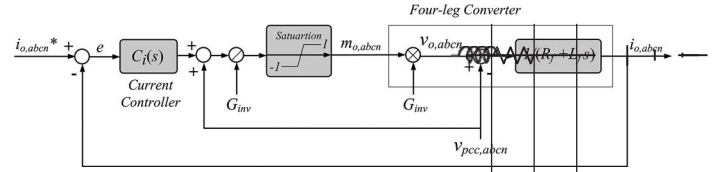


Fig. 5. Block diagram of the current control loop.

ω_z , ω_p , and k_c are the zero, pole, and the gain of the compensator, respectively. Furthermore, the voltage feed-forward compensation is employed to mitigate the dynamic couplings between the four-leg inverter and the ac system, enhancing the disturbance rejection capability of the converter system

$$L_f \frac{di_{o,abcn}(t)}{dt} + R_f i_{o,abcn}(t) = v_{o,abcn}(t) - v_{pcc,abcn}(t). \quad (16)$$

$$v_{o,abcn}(t) = G_{inv} m_{o,abcn}(t) = \frac{V_{dc}}{2} m_{o,abcn}(t). \quad (17)$$

$$G_i(s) = \frac{i_{o,abcn}(s)}{v_{o,abcn}(s)} = \frac{1}{L_f s + R_f} \quad (18)$$

$$G_{oi}(s) = \frac{C_i(s)}{R_f + sL_f}, \quad (19)$$

$$C_i(s) = \frac{k_c}{1 + s/\omega_p} \left(1 + \frac{s}{\omega_z} \right). \quad (20)$$

For DSP implementation of the control system, in the next step, it is suggested to convert the functions of continuous plane “s” to the discrete plane “z”. The Plant transfer function in z-domain is obtained by means of the z-transformation. The z-transformation of a transfer function in s-domain, combined to a zero-order holder, is given by (21). Transformation is made using the relation $z = e^{s.T_a}$. So, $G_i(z)$ can be defined as follows [24]:

$$G_i(z) = Z \left\{ \frac{1 - e^{-s.T_a}}{s} G_i(s) \right\}. \quad (21)$$

$$G_i(z) = 1 - z^{-1} Z \left\{ \frac{G_i(s)}{s} \right\}. \quad (22)$$

To allow the use of the frequency response method design, the conversion of $G_i(z)$ transfer function from “z” plane to “w” plane is performed using the bilinear transform shown in (23)

$$z = \frac{1 + \frac{T_a}{2} w}{1 - \frac{T_a}{2} w}. \quad (23)$$

From where comes

$$G_i(w) = \frac{-0.0041w + 100}{w + 10}. \quad (24)$$

Fig. 6 presents a comparison between the frequency response of system transfer function $G_i(s)$, and digitalized plant $G_i(w)$. It is noticeable that the frequency response presents conformity

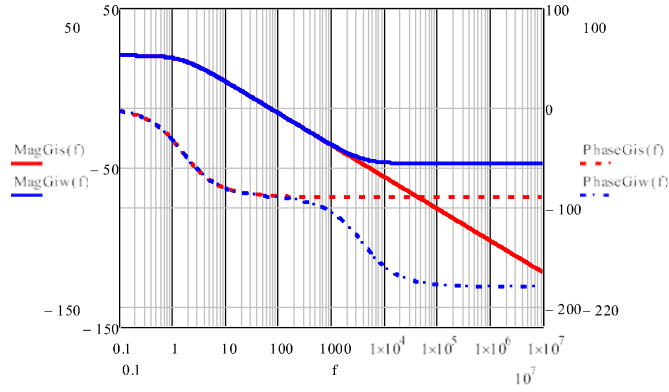


Fig. 6. Gain and the phase of the current control plant in both “s” and “w” planes.

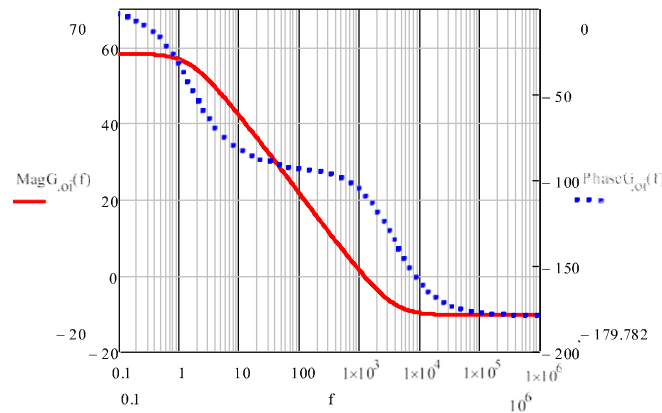


Fig. 7. Bode plot of the open-loop current transfer function.

up to 3 kHz, when the phase error goes by substantial caused by the zero added because of the digitalization process.

The crossover frequency of the current controller is chosen to be one-tenth of switching frequency. For $f_{ci} = 1.2$ kHz, $\phi_{PMi} = 72^\circ$, and $f_z = f_{ci}/10 = 120$ Hz, the rest of parameters in (20) are calculated as $f_p = 106.6$ Hz and $k_c = 80.88$. The frequency response of the open-loop transfer function is illustrated in Fig. 7. It can be seen that at crossover frequency, the open loop gain of 0 dB and the phase margin of 72° are obtained.

The output current behavior of the grid-tied four-leg inverter can be described by (25). It can be seen that the output current only depends on the reference current. In other words, under the feed-forward compensation, the converter system is equivalent to an independent current source as viewed by the ac system

$$i_{o,abcn}(s) = \frac{C_i(s)}{L_f s + R_f + C_i(s)} i_{o,abcn}^*(s). \quad (25)$$

For digital implementation of the control system in the z-domain, the controller of (20) is discretized by the bilinear transform with a sampling time of T_s that is also the switching period [24]. Therefore, the controller transfer function $C_i(z)$

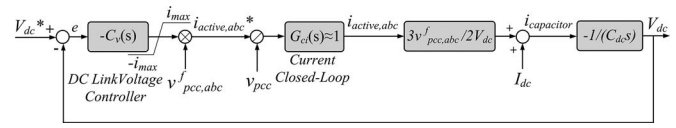


Fig. 8. Block diagram of the dc voltage control loop.

can be expressed as (26)

$$C_i(z) = \frac{72.1z - 67.7}{z - 0.94}. \quad (26)$$

The current reference, $i_{active,abc}$, is used to inject the active power delivered from the wind through the inverter. The waveform of the active current reference is defined from the fundamental component of the measured load voltage, $v_{pcc,abc}^f$, configuring sinusoidal current. Therefore, the active current is a pure sinusoidal current, in phase with the fundamental component of the instantaneous load voltage. Dimensioning of the dc-link voltage controller is determined by the transfer function between the defined current reference and the dc-link voltage.

From power balance of the inverter terminal, we have

$$P_{ac} + P_{wind} + P_{cap} = 0. \quad (27)$$

$$\frac{3}{2} v_{pcc,abc}^f i_{active,abc} + V_{dc} I_{dc} + V_{dc} i_{capacitor} = 0. \quad (28)$$

where $i_{capacitor}$ is the dc-link capacitor current and 3/2 factor comes from the average ac power flow using peak values and $v_{pcc,abc}^f$ represents the fundamental component of the PCC voltage.

From (28) the current through the capacitor is

$$i_{capacitor} = - \frac{3v_{pcc,abc}^f i_{active,abc}}{2V_{dc}} + I_{dc}. \quad (29)$$

The same current in terms of voltage across the capacitor is given by

$$C_{dc} \frac{dV_{dc}}{dt} = i_{capacitor}. \quad (30)$$

From (29) and (30), the differential equation for the dc-link voltage becomes

$$\frac{dV_{dc}}{dt} = - \frac{3v_{pcc,abc}^f i_{active,abc}}{2C_{dc} V_{dc}} + I_{dc}. \quad (31)$$

Based on (31) the dc voltage is regulated by controlling the active current $i_{active,abc}$. The block diagram of the dc voltage control loop is shown in Fig. 8. The dc-link voltage controller $C_{vdc}(s)$ is multiplied by -1 to compensate for the negative sign of dc bus voltage dynamics. We will select the bandwidth of dc voltage loop to be less than two orders of magnitude smaller than that of the current loop.

Therefore, the closed current loop can be assumed ideal for design purposes and replaced by unity. The transfer functions of dc-link voltage control scheme, $G_{vdc}(s)$, is presented in (32). The open-loop transfer functions of the dc voltage control loop, $G_{ovdc}(s)$, is presented in (33) with $C_v(s)$ the controller

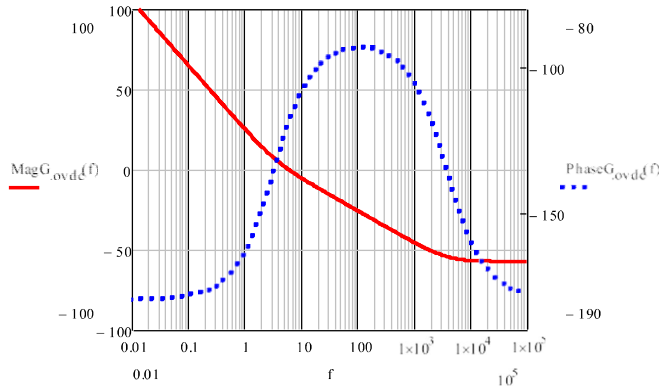


Fig. 9. Bode plot of the open loop dc-link voltage transfer function.

of the dc voltage control loop, consisting of a proportional integral compensator as in (34), where the parameters of k_p and k_i are the proportional and integral gains of the compensator, respectively,

$$G_{vdc}(s) = \frac{3v_{pcc,abc}^f}{2V_{dc}} \frac{1}{C_{dc}s} \quad (32)$$

$$G_{ovdc}(s) = C_v(s) G_{vdc}(s) \quad (33)$$

$$C_v(s) = \frac{k_p s + k_i}{s} \quad (34)$$

For DSP implementation of the dc-link voltage control scheme, $G_{vdc}(s)$, is converted from continuous plane “s” to the discrete plane “z” in (35). To allow the use of frequency response method design, the conversion of $G_{vdc}(z)$ transfer function from “z” plane to “w” plane in (36) is performed, using the bilinear transform of (23)

$$G_{vdc}(z) = \frac{1 - z^{-1}}{z} Z \left[\frac{G_{vdc}(s)}{s} \right] \quad (35)$$

$$G_{vdc}(w) = \frac{-0.00225w + 54}{w} \quad (36)$$

The crossover frequency of the dc voltage loop is chosen to be $f_{c vdc} = 6$ Hz and the phase margin ϕ_{PMvdc} is selected to be 60° . We can compute that $k_p = 0.6$ and $k_i = 13.12$. Fig. 9 shows the frequency response of the open-loop dc-link voltage control scheme. It can be seen that at cross over frequency, the open loop gain of 0 dB and the phase margin of 60° are obtained.

The dc-link voltage controller $C_v(s)$ is also discretized for digital implementation using the bilinear transform with a sampling time of T_s that is also the switching period [24]. Therefore, the controller transfer function $C_v(z)$ can be expressed as follows:

$$C_v(z) = \frac{0.6z - 0.6}{z - 1} \quad (37)$$

IV. REAL-TIME SIMULATION AND HARDWARE IN THE LOOP RESULTS

The proposed industrial system with the wind turbine shown in Fig. 1 was modeled and compiled using the well-known real-time simulator Opal-RT. Opal-RT allows precise bench-

marking of real-time controllers, with specific sampling for specific control blocks. After an Opal-RT study such as this one, it is possible to generate C code for accurate compilation on real-time kernels or real-time operating systems, usually implemented with DSP hardware.

The PMSG parameters used in the model are taking from [25]. The specification of the wind turbine was selected in accordance to those parameters. The wind turbine has an optimum wind speed of 200 r/mIN at 10-m/s rated wind speed. The load parameters listed in Table II are used in the model.

The control algorithm was implemented using HIL. The wind turbine model with the grid connected back-to-back converter and power grid were built inside Matlab/Simulink. Then, the system was compiled inside the real-time simulator “Opal-RT.” The control of the grid-side converter was implemented in the co-processor DSP (TI TMS230F28335), outside the Opal-RT system. The CPT theory was coded inside the DSP along with the current controllers. A sampling frequency of 12 kHz is used to discretize the signals. The test is implemented for various cases. The scaling for phase voltages, phase, and neutral currents per division are 60 V, 15 A and 5 A, respectively.

A. Active Power Delivery

In this case study, the four-leg inverter is set to deliver active power produced by the wind to the load, ($i_{ref} = i_{active}$), and the remaining active power is delivered to the grid with unity power factor without doing any compensation strategy. Fig. 10(a) shows the inverter voltage is in phase with the inverter current meaning only active power is delivered to the load and grid. From Fig. 10(b), the grid currents are unbalanced and distorted showing the requirement for power quality improvement. In Fig. 10(c), it is clear that the utility is supplying the linear and nonlinear single loads through its neutral wire while the inverter neutral current is zero.

B. Active and Reactive Power Delivery

In Fig. 11, the controller is set to supply the balance reactive current/power component of the load besides the delivery of active power ($i_{ref} = i_{active} + i^b$). From the voltage and current waveforms shown in Fig. 11(a), the inverter is supplying active and reactive power since the inverter current is no longer in phase with the voltage. The result of this compensation strategy is shown in Fig. 11(b) in which the void and unbalance current components of the load is supplied by the grid. It can be seen from Fig. 11(c) the grid is supplying the neutral current, related to single phase loads.

C. Active Power Delivery and Unbalance Compensation

The load considered in the system imposes unbalance component to the grid’s current. Therefore, the CPT, proposed in the paper, is used to extract the unbalance current/power component of the load. In this study, the aim is to compensate the unbalance current component caused by the single- and intraphase loads ($i_{ref} = i_{active} + i^u$). Therefore, the inverter current is sinusoidal but unbalanced whereas the grid currents are

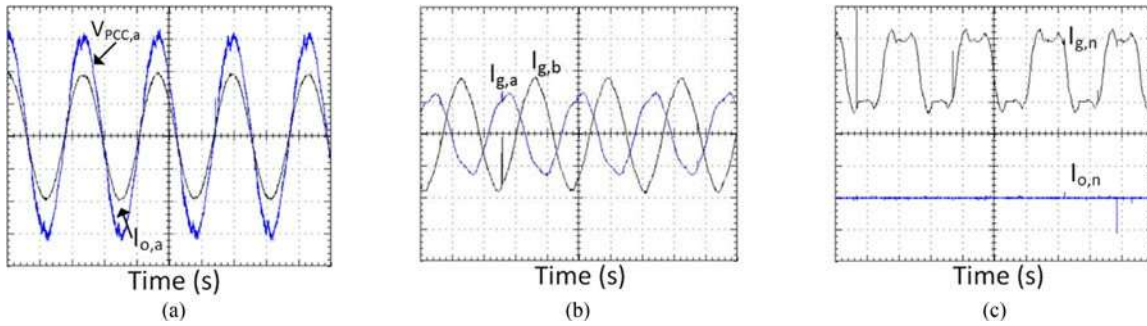


Fig. 10. Active power delivery: (a) PCC voltage and inverter current; (b) two phases of grid currents; and (c) grid neutral current ($I_{g,n}$) and inverter neutral current ($I_{o,n}$).

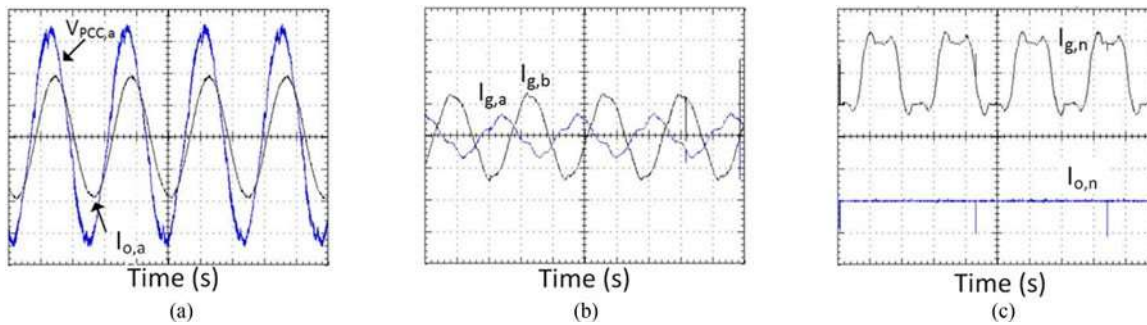


Fig. 11. Active and reactive power delivery: (a) PCC voltage and inverter current; (b) two phases of grid currents; and (c) grid neutral current ($I_{g,n}$) and inverter neutral current ($I_{o,n}$).

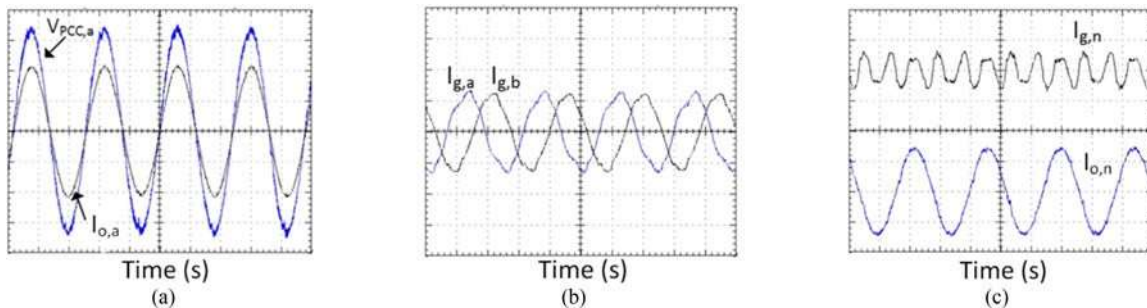


Fig. 12. Active power delivery and unbalance compensation: (a) PCC voltage and inverter currents; (b) two phases of grid current; and (c) grid neutral current ($I_{g,n}$) and inverter neutral current ($I_{o,n}$).

balanced but nonsinusoidal and out of phase with the voltages as shown in Fig. 12(a) and (b) respectively. In this case, the inverter current is responsible for supplying unbalance component of the single phase loads through its fourth-leg as it is illustrated in Fig. 12(c). Note that the harmonic current component of the single- and three-phase loads is still supplied by the grid.

D. Active Power Delivery and Harmonics Compensation

At this case study, the inverter is providing harmonics compensation by injecting the void currents ($i_{ref} = i_{active} + i_v$). From Fig. 13(a) and (b), the inverter current is nonlinear whereas the grid current is sinusoidal but unbalanced and not in phase with the voltages. It can be observed that the grid in this case is

not supplying the single-phase void current components through its neutral wire rather it is supplied by the inverter through its fourth-leg as illustrated in Fig. 13(c). The neutral wire of the grid carries only the unbalance current component related to the single-phase loads.

E. Active Power Delivery and Nonactive Compensation

In Fig. 14, the inverter is set to compensate nonactive current component of the load current including all disturbances, i.e., load reactive power, nonlinearities, and unbalances ($i_{ref} = i_{active} + i_{na}$). Fig. 14(a) shows that the inverter current contains nonactive current component, whereas Fig. 14(b) shows the grid is absorbing the remaining active current which is not consumed by the load. Note that the active current, exported

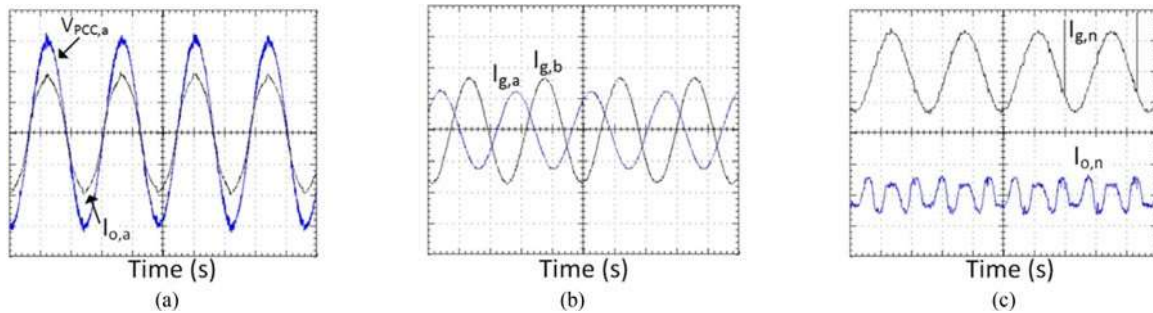


Fig. 13. Active power delivery and void compensation: (a) PCC voltage and inverter currents; (b) two phases of grid current; and (c) grid neutral current ($I_{g,n}$) and inverter neutral current ($I_{o,n}$).

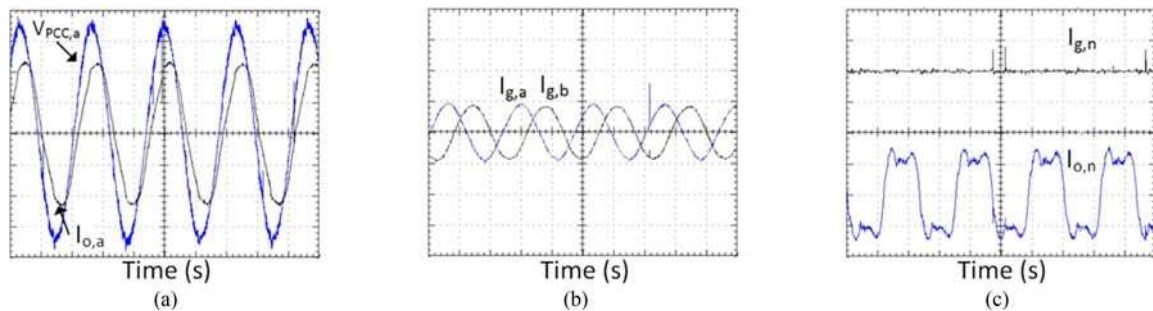


Fig. 14. Active power delivery and nonactive compensation: (a) PCC voltage and inverter currents; (b) two phases of grid current; and (c) grid neutral current ($I_{g,n}$) and inverter neutral current ($I_{o,n}$).

SOFTWARE DESIGN AND SIMULATION RESULTS

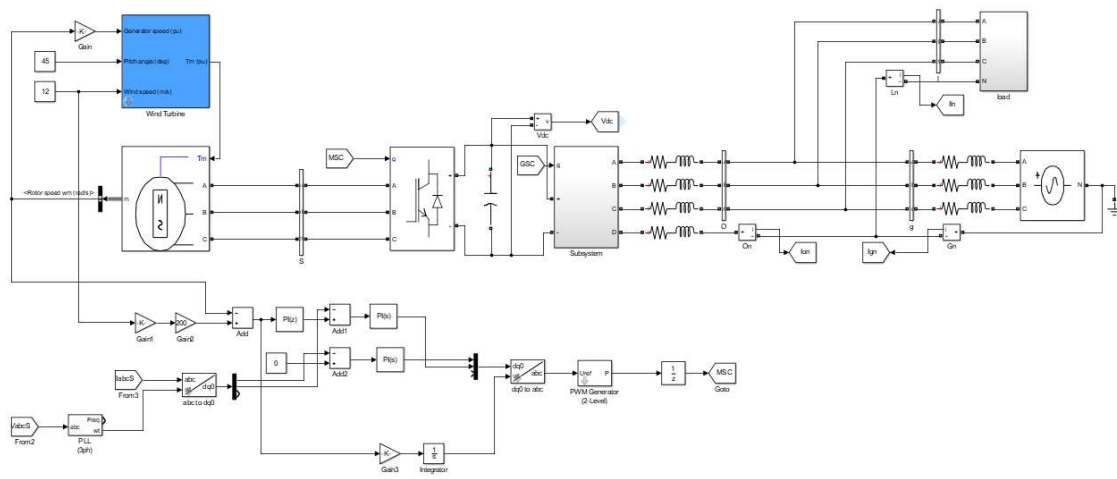


Fig. Simulink model of Proposed System

The simulation model of proposed system is designed in Matlab2016a and the results consists of Active power delivery and non compensation at $t=7s$, Active power delivery and nonactive compensation under different wind speeds, Spectrum and THD of grid current without power

quality improvement: (a) phase-a; (b) phase-b; and (c) phase-c. and Spectrum and THD of grid current with nonactive compensation: (a) phase-a; (b) phase-b; and (c) phase-c.

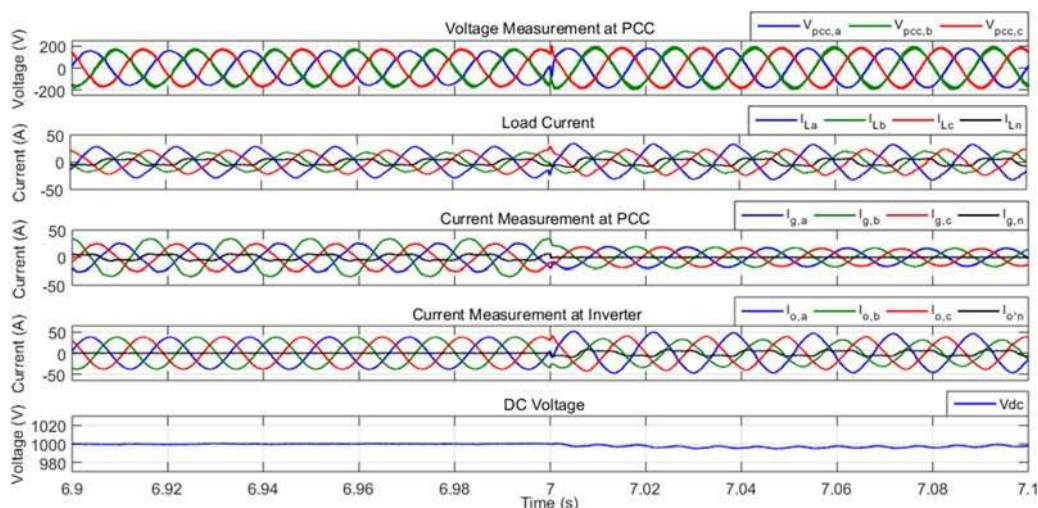


Fig. 15. Active power delivery and nonactive compensation at $t = 7$ s

to the grid is proportional to the instantaneous PCC voltages. As shown in Fig. 14(c), the grid supplies zero current through its neutral and the inverter is supplying the return current of single phase loads through its fourth-leg.

F. Multifunctional and Active Filter Modes

In this section, two different tests are performed to validate the overall performance of the machine side and the grid side controllers during different wind speed conditions.

In Fig. 15, a test is done to validate the controller when it switches from active power delivery only to active and non-active compensation at maximum wind power. From Fig. 15, at $t = 7$ s, the inverter started providing active power as well as nonactive compensation. The dc-link voltage starts to oscillate but kept at its desired value. The grid current becomes sinusoidal and balanced. The inverter current, on the other hand, becomes unbalanced and nonlinear. The neutral current is produced by the fourth leg of the inverter resulting in zero neutral current at the grid side.

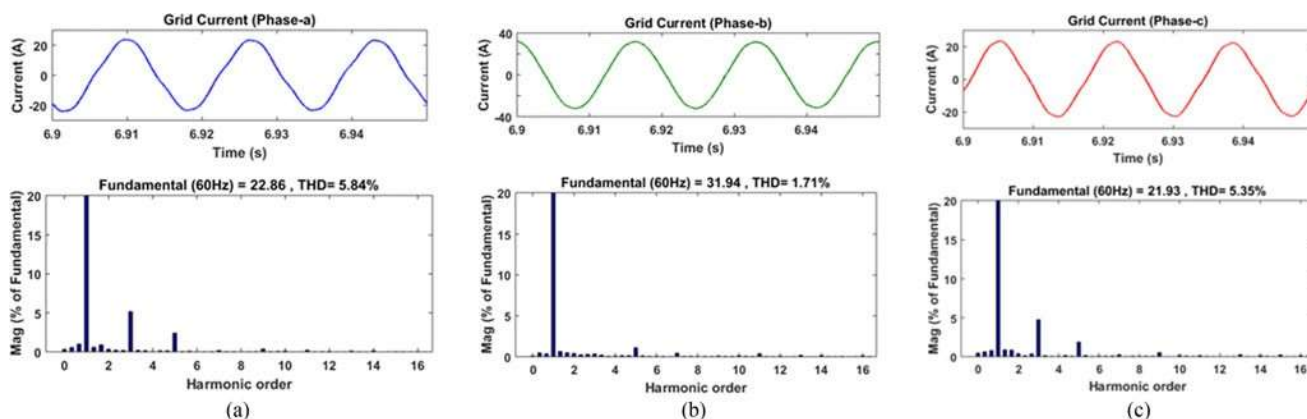


Fig 16. Spectrum and THD of grid current without power quality improvement: (a) phase-a; (b) phase-b; and (c) phase-c.

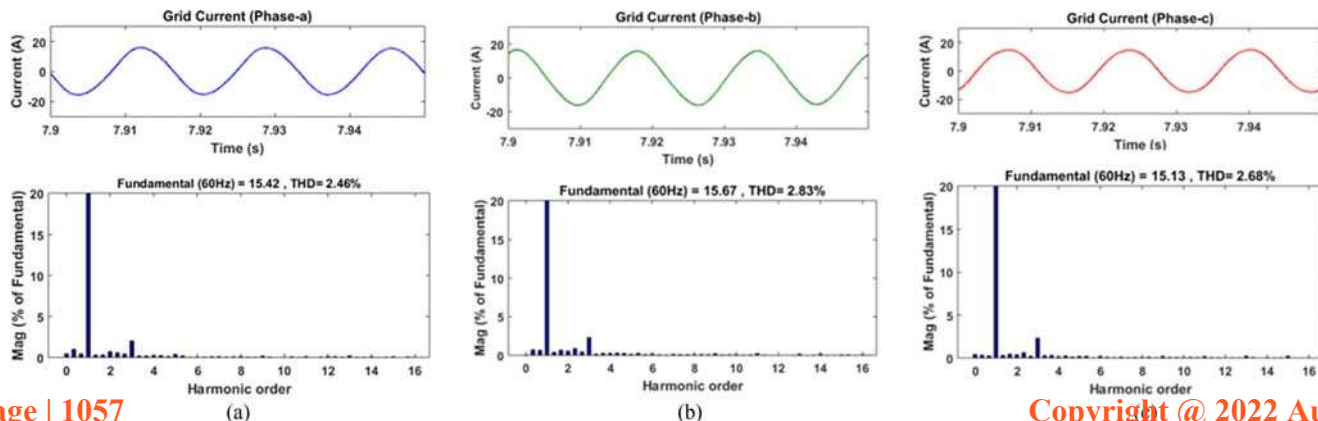


Fig. 17. Spectrum and THD of grid current with nonactive compensation: (a) phase-a; (b) phase-b; and (c) phase-c.

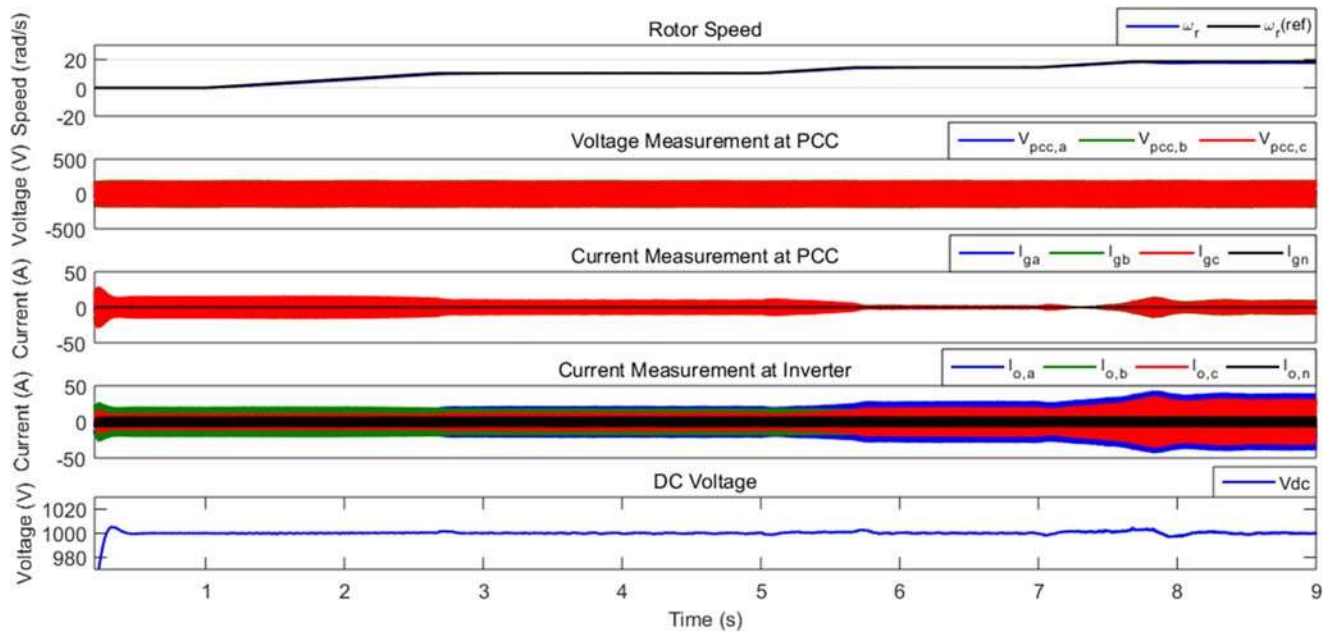


Fig. 18. Active power delivery and nonactive compensation under different wind speeds.

The harmonics spectrum of the grid current and total harmonic distortion (THD) with no compensation is shown Fig. 16. Since there are single- and three-phase loads as well as intraphase loads in the system, the THD is different for each phase. The current of phase-a and phase-c contain THD of 5.84% and 5.35%, respectively.

In Fig. 17, the grid current spectrum is demonstrated after the inverter is set to compensate the load nonactive current components. The THD of phases-a and phase-c were reduced from 5.84% and 5.35% to about 2.46% and 2.68%, respectively. Phase-b initially had much less harmonics because it does not have nonlinear single-phase load as the other phases. The amplitude of the grid current is reduced as the inverter is also supplying the unbalance components.

In Fig. 18, a comprehensive test is performed under different wind speeds. At no wind available or zero rotor speed, the grid-side inverter is operating as active filter. Therefore, the controller is intended to keep the dc voltage at constant value (1000 V) and provide nonactive compensation to improve the power quality of the grid current. During this condition, the grid supplies the active power for the load. When the wind speed increases above the cut-in speed and the turbine started producing power, the grid-side inverter injects the active and compensates nonactive components. If the produced power is more than the load power, the remaining is injected to the grid. During all the time, the dc-link voltage is kept constant at 1000 V.

V. CONCLUSION

This paper addressed a comprehensive control method for a back-to-back wind turbine system connected to an industrial plant. The control uses the four-leg inverter at the grid side to supply available active power from the wind turbine system along with full compensation of load current disturbances. The main contribution is based on CPT to impress the set-point reference and impose disturbances mitigation, which adds significant flexibility to the control structure.

The control structure was tested with a comprehensive real-time benchmarking case-study with hardware in the loop. The control algorithms were compiled inside our TI DSP and validated using the real-time system “Opal-RT.” The algorithms were debugged and are ready for experimental validation in a retrofitting of a wind turbine (future work). The results showed good performance of the algorithm and the THD was improved for all different operation conditions. The results support the system presented here which can avoid installation of active filter hardware by the utility or by the industrial consumer.

REFERENCES

- [1] “Global wind report annual market update 2013,” 2013. [Online]. Available: <http://www.gwec.net>
- [2] S. Li, T. A. Haskew, R. P. Swatloski, and W. Gathings, “Optimal and direct-current vector control of direct-driven PMSG wind turbines,” *IEEE Trans. Power Electron.*, vol. 27, no. 5, pp. 2325–2337, May 2012.
- [3] N. Angela, M. Liserre, R. A. Mastromauro, and A. D. Aquila, “A survey of control issues in PMSG-based,” *IEEE Trans. Ind. Informat.*, vol. 9, no. 3, pp. 1211–1221, Aug. 2013.
- [4] J. Lagorse, M. G. Simões, and A. Miraoui, “A multiagent fuzzy-logic-based energy management of hybrid systems,” *IEEE Trans. Ind. Appl.*, vol. 45, no. 6, pp. 2123–2129, Nov./Dec. 2009.
- [5] X. Tan, Q. Li, and H. Wang, “Advances and trends of energy storage technology in microgrid,” *Int. J. Elect. Power Energy Syst.*, vol. 44, pp. 179–191, Jan. 2013.